6th African School on Electronic Structure Methods and Applications (ASESMA-2021) | (SMR 3578)

31 May 2021 - 11 Jun 2021
Virtual, Virtual, Italy

P01 - ACHEHBOUNE Mohamed

First principal calculations on the electronic and optical properties of Er doped ZnO: effect of Er concentration and intrinsic defects

P02 - AGBAOYE Ridwan Olamide

Electronic and Optical absorption spectra of Ferromagnetic Co3O4

P03 - BALOGUN Rilwan Oluwanishola

First-principles calculations to investigate structural, electronic and optical Properties of MgHfS3

P04 - CHIKA Khouloud

Injection of charges in the organic solar cells

P05 - FANKAM FANKAM Jean Baptiste

Study of Electronic Structure, Optoelectronics, Linear and Nonlinear Optical Properties and chemical descriptors of Dibromodinitrofluorescein Isomers in Gas Phase and Solvent media Using Ab Initio and DFT Methods

P06 - ISAMBULA Imani Sospeter

Quantum Chemical Study of Structure, Vibrational Spectra and Thermodynamic Properties of Molecular and Ionic Clusters Existing in Vapours over Strontium Dichloride,

P07 - KHAEMBA Kennedy Wamalwa

Tantalum phosphide: A topological weyl semimetal.

P08 - KING'ORI Wangechi Gladys

Ab initio insights into Graphene-Zirconium disulfide/diselenide heterostructure as electrode material for alkali-ion batteries

P09 - MORAD Razieh

Enhancement of curie temperature of Dysprosium deposited on BN monolayer

P10 - MULWA Mueni Winfred

Magnetic properties of stable iron based compounds

P11 - NKOU Falonne Bertholde Sharone

Theoretical insights into magnetization in graphene containing single and interacting nanoporous defects

P12 - OKELLO Alex

Influence of concentration of anthocyanins on electron transport in dye sensitized solar cells

P13 - SIFUNA James Simiyu

Quasi-two-dimensional electron and hole gases at the head-to-head and tail-to-tail 180° domain walls in ferroelectric thin films

P14 - TSHWANE David Magolego

Computational study of chlorine-ion adsorption on Ti (100) surface

P15 - WOLDEMARIAM Mengesha Menberu

Structural and Electronic Calculation of Tungsten Disulfide Using Density Functional Theory

P16 - ASHANI Timothy

Thermoelectric Properties, Effective Mass and Fitness function in CuSbS2: Density Functional Theory Approach

First principal calculations on the electronic and optical properties of Er doped ZnO: effect of Er concentration and intrinsic defects

M. achehboune[1,2], M. Khenfouch[2], I. Boukhoubza[1,2], I. Derkaoui[1,2], B. M. Mothudi[3], I. Zorkani[1], A. Jorio[1]

[1]Sidi Mohammed Ben Abdellah University, Faculty of Sciences Dhar el Mahraz, Laboratory of Solid State Physics, Group of Nanomaterials and Renewable Energies, PO Box 1796 Atlas Fez 30 000, Morocco.
[2]Africa Graphene Center, Department of Physics, College of Science, Engineering and Technology, Science Campus, University of South Africa, Cnr Christiaan de Wet & Pioneer Avenue Florida 1709, Johannesburg, South Africa.
[3]University of South Africa, Department of Physics, Private Bag X90, Florida, 1710, South Africa.

Corresponding author: achehboune.mohamed01@gmail.com

Abstract.

In this study, we evaluate the structural, electronic and optical properties of Er-doped ZnO with various concentrations of Er, as well as the effect of native defects in Er-ZnO by using the GGA + U method based on the first-principles method. Our calculations show that the band gap of Er-doped ZnO decreases with increasing Er concentration while it increases with the presence of oxygen or zinc vacancies. In addition, the existence of Vo in ZnO-Er caused the formation of a deep donor level in the band gap. However, the Er-ZnO+VZn is a degenerate p-type semiconductor, and shallow acceptor states were created around the Fermi level in the VBM, increasing the carrier concentration. The absorption properties relatively enhanced in the visible range after doping with Er as well as with the presence of oxygen vacancy. In the Er-ZnO+V_O model, absorption and reflection are both relatively enhanced in the visible range, leading to a decrease in light transmittance. High transmittance in the UV-visible region was observed in the Er doped ZnO with an optimum concentration of 4.17%. The optoelectronic properties of ZnO can be improved by suitable Er doping with an optimal concentration of 4.17% as well as with the presence of oxygen vacancies which could be suitable for detector and sensor applications

Keywords: Er-doped ZnO, native defects, First-principles, Electronic structure, Optical properties.

Electronic and Optical absorption spectra of Ferromagnetic Co3O4

Co3O4 is famous for its interesting electronic structure and optical absorption, making it suitable for several technological applications. We modelled the minimum energy configuration of cubic Co3O4 in the ferromagnetic phase by optimizing the lattice structure and the ionic position. The electronic structure was calculated using the Perdew-Burke-Enzenhoff exchange-correlation functional within the generalized gradient approximation of the density functional theory with and without Hubbard correction and the GW quasiparticle method. At the same time, the absorption spectra were determined by solving the Bethe-Salpeter equation. The underestimated upspin, and downspin density functional theory bandgap was reported, while the upspin and downspin bandgaps correction was calculated using the density functional theory with Hubbard correction and the GW quasiparticle methods. The hybridization of oxygen (O) p orbital and cobalt (Co) d orbital contribute to the valence band around the Fermi level, while the cobalt (Co) d orbital is most responsible in the conduction band around the Fermi level. Absorption coefficient and spectroscopic limited maximum efficiency results indicate an exciting prospect for solar cell absorber.

First-principles calculations to investigate structural, electronic and optical Properties of MgHfS3

The development of a non-toxic, efficient, cheap, and emerging class of semiconductor as solar absorber is vital for photovoltaic applications. Magnesium Hafnium sulfide, MgHfS3 has properties which makes it chalcogenide perovskite for optoelectronic applications. Here, we present first-principle calculation method, based on the density functional theory (DFT) and the plane-wave method as implemented in the Quantum Espresso package has been used to obtain the structural, electronic, and optical properties of MgHfS3. From the analysis, the band structure shows that the material is an indirect bandgap material with a value of 1.43eV, in close agreement with estimates of refractive index, reflectivity and extinction coefficient. A strong optical absorption coefficient of the order of 108 cm-1 with wavelength of 540nm in the visible region was predicted, the reflectivity of 0.52, the refractive index of 4.3, and extinction coefficient of 4.7 show the optical credibility of the material when compared to other chalcogenide and halide perovskites. Hence, an attractive non-toxic, stable, and cost-effective material for photovoltaic application.

Injection of charges in the organic solar cells

Khouloud Chika[1], Jouda Jemaa Khabthani[1], and Didier Mayou[2]

[1] *(Laboratoire de Physique de la Matière Condensée,Département de Physique,Faculté des Sciences de Tunis, Université Tunis El Manar, Campus Universitaire,1060 Tunis,Tunisia)*

[2] *CNRS, Institut NEEL, F-38042 Grenoble, France.Université Grenoble Alpes,Institut NEEL, F-38042 Grenoble, France*

In an organic solar cell, several physical processes are poorly understood, which makes it difficult to understand the low efficiency in this type of cell. This requires doing a quantum study. At the interface between the donor molecule and the acceptor molecule, there is a competition between the separation of charges at the donor-acceptor interface and the recombination of the electron with the hole. It is a question of modeling this system taking into account all the physical phenomena and based on Green's function. The model used to study the charge injection is the Bethe lattice.

Study of Electronic Structure, Optoelectronics, Linear and Nonlinear Optical Properties and chemical descriptors of Dibromodinitrofluorescein Isomers in Gas Phase and Solvent media Using Ab Initio and DFT Methods

In this work, we have studied the electronic structure, optoelectronics, linear and nonlinear optical properties of dibromodinitrofluorescein isomers in the gas phase and some solvents media using RHF and B3LYP levels of theory with a cc-pVDZ basis set. Our results suggest that solvent media have an effect on certain properties while some are unaffected. We have also determined the energy band gap and some other parameters like ionization potential, electron affinity, and molar refractivity. Finally, we have calculated the reactivity descriptors through some parameters including chemical hardness, chemical potential, electrophilicity index (E F), Electro accepting power, reflectivity, softness, electronegativity (EN), Fermi energy, electron-donating power, optical frequency, and total Energy minimum and net electrophilicity, Max of Electron charge, Energy of the compounds. Due to the large $\langle\alpha\rangle$, β, γ, E, P, χ, $\mathcal{E}$, n, and D of these molecules, we think that these molecules have potential applications in the field of optoelectronics, such as optical communication, optical computing, optical switching, and dynamic image processing.

ABSTRACT

The equilibrium geometrical properties, vibrational spectra and thermodynamic properties of the cluster ions $SrCl_3^-$, $Sr_2Cl_3^+$, $Sr_3Cl_5^+$, $Sr_4Cl_7^+$ and $Sr_5Cl_9^+$ that were detected earlier in vapour over strontium dichloride at high temperature ranging from 1100 – 1500 K were determined. The Density Functional Theory (DFT/B3P86), and the second, and the fourth order Møller – Plesset perturbation theory (MP2 & MP4) were applied to characterize the geometrical structures, vibrational spectra and thermodynamic properties of cluster ions. The B3P86 and MP2 methods consist of effective core potential, for strontium atom, def2-TZVP basis set was used while for chlorine atom two basis sets namely midsized basis set, McLean-Chandler (MC) denoted as B1 and extended basis set, aug-cc-pvtz denoted as B2 were used. The effect of the computational methods and basis sets were established through comparison of theoretical results and experimental results for simple species obtained from literature. Alternative structures of the cluster ions were studied but no isomers were identified. The cluster ions $SrCl_3^-$, $Sr_2Cl_3^+$, $Sr_3Cl_5^+$, and $Sr_5Cl_9^+$ were confirmed to correspond to D_{3h} symmetry group and $Sr_4Cl_7^+$ to C_{2v} configuration. The vibrational frequencies and structural properties computed with B3P86 and MP2 observed to be not much sensitive to the basis set used.

The enthalpies of dissociation reactions for the cluster ions were determined both theoretically through the total energies and ZPVE of the participant species and based on experimental data obtained through treatment of equilibrium constants measured earlier for cluster ions, $Sr_2Cl_3^+$ and $Sr_3Cl_5^+$. The enthalpies of dissociation reactions, $\Delta_r H^0(0)$ were determined (in KJmol^{-1}): 280 ± 3 ($SrCl_3^-$), 330 ± 12 ($Sr_2Cl_3^+$), 329 ± 16 ($Sr_3Cl_5^+$), 276 ± 27 ($Sr_4Cl_7^+$), and 273 ± 20 ($Sr_5Cl_9^+$). Also, enthalpies of formation, $\Delta_f H^0(0)$ of the cluster ions were determined (in KJmol^{-1}): -994 ± 3 ($SrCl_3^-$), -410 ± 12 ($Sr_2Cl_3^+$), -1202 ± 16 ($Sr_3Cl_5^+$), -1962 ± 27, and -2718 ± 20. The theoretical data of $\Delta_r H^0(0)$ and $\Delta_f H^0(0)$ for the ions $Sr_2Cl_3^+$ and $Sr_3Cl_5^+$ give good agreements with experimental data 'based on experiment'.

Tantalum phosphide: A topological weyl semimetal.

Topological semi-metals are newly discovered states of quantum matter that have arose interest in the research community due to their application in spintronics and valleytronics- ics. There are three types of topological semi-metals (TSMs); Dirac Semi-metal (DSM), Weyl Semi-metal (WSM) and Node Line Semi-metal (NLSM), each with special features that makes them novel candidates for future technologies. Unlike topological insulators (TI) that have an energy gap, TSMs have their valence and conduction bands touching in discrete points in the Brillouin zone. Tantalum phosphide (TaP), has been classified as a Weyl semi-metal with only a single type of Weyl fermions and thus topologically distinguished from tantalum arsenide (TaAs) that has two types of Weyl fermions. Theoretically, if spin-orbit interaction is turned on in the system, we expect an energy gap. To this date, little has been devoted to this relativistic interaction in TaP. Our goal will be to calculate the band- structure in TaP and how the spin-orbit interaction alters the single Weyl fermions. We will employ first-principles density functional theory (FPDFT) as implemented in Siesta code. This study is not only based on fundamental research interests but also of great potential for future applications.

Ab initio insights into Graphene-Zirconium disulfide/diselenide heterostructure as electrode material for alkali-ion batteries

In the search for an energy storage medium with higher electronic conductivity, rate performance and moderate volume expansion, van der Waals heterostructures are a promising alternative. Herein, the potential of graphene (Gr) and Zirconium dichalcogenide (ZrX_2, X= S, Se) van der Waals heterostructures for applications as battery electrodes is explored using density functional theory (DFT) calculations. Through intercalating alkali ions (Li and K) between the Gr and ZrX_2, we obtain low energy activation barriers, indicating that Gr-ZrX_2 van der Waals heterostructures can be candidates for high rate performance electrode application. DFT calculations also indicate that the Gr-ZrX_2 heterostructure formation is energetically favoured with better volume expansion as compared to bilayer Gr and ZrX_2. The calculated open circuit voltage (OCV) for K intercalation was 0.66 V (Gr-$ZrSe_2$) and 0.77 V (Gr-ZrS_2), hence suitable for anodic application in Potassium-ion batteries (KIB). The calculated OCV for Li interaction was 2.83 V (Gr-$ZrSe_2$) and 2.95 V (Gr-ZrS_2) hence suitable for cathodic applications.

Enhancement of curie temperature of Dysprosium deposited on BN monolayer

Experimental results indicate the enhancement of Curie Temperature of Dysprosium (Dy) nanoparticle deposited on hBN monolayer. Our preliminary DFT simulations predicted the Curie temperature of bulk Dy about 83 K, which is reasonably close to the experimental data ~ 88 K. In this work, we aim to calculate the enhancement of magnetism and Curie temperature of Dy NPs using the DFT and some atomistic Monte Carlo simulations.

Magnetic properties of stable iron based compounds

Winfred Mueni Mulwa[1]

[1] Department of Physics, Egerton University, P.O Box 536-20115 Egerton, Kenya

winfred.mulwa@egerton.ac.ke

Magnetic stability is considered as the constant magnetic production by a magnetic compound when subjected to a peculiar environment. Iron based compounds are known to be the best in magnetic production, therefore there is need for investigation on which of the stable iron based compounds is the best candidates for this production. In this study, $FeMnP_{0.67}Si_{0.33}$ is taken as the base compound. This compound has been studied as one of the stable iron based compounds, but it exhibits some mechanical instability. In this work, $FeMnP_{0.67}Si_{0.33}$ was optimized and its magnetic properties examined in both ferromagnetic and antiferromagnetic phases. Silicon Si was substituted with selected elements in period 4 and 5 which have shown first order magnetic transition at near room temperature. Selenium Se and Tin Sn were used to substitute Si in this case. These two elements were used due to their availability and non-toxic nature. Generalized gradient approximation (GGA) within the Density Functional Theory (DFT) formalism was utilized. The calculated results indicated that only the ferromagnetic phases of both the base as well as the doped compounds displayed encouraging magnetic properties. It was realized that, starting magnetization of $1.0\mu B$ was the most stable state within a minimum energy of -1425.57280534 Ry. Also, the total local magnetic moment per cell reduced from $9.81\mu_B$ in the ferromagnetic phase to $0.00\mu B$ in the antiferromagnetic phase of $FeMnP_{0.67}Si_{0.33}$.

Theoretical insights into magnetization in graphene containing single and interacting nanoporous defects

F. B. S. NKOU[1], D. H. Douma[1], B. R. Malonda-Boungou[1,2], B. M'passi-Mabiala[1,2], A. T. Raji[3], and S. Kenmoe[4]

[1]Groupe de Simulations Numériques en Magnétisme et Catalyse, Faculté des Sciences et Techniques, Université Marien Ngouabi, B.P. 69, Brazzaville, Congo
[2]Unité de Recherche en Nanomatériaux et Nanotechnologies, Institut National de Recherche en Sciences Exactes et Naturelles (IRSEN), Brazzaville, Congo
[3]Department of Physics, College of Science, Engineering and Technology (CSET), University of South Africa (UNISA-Florida Campus), Corner of Christiaan de Wet Road & Pioneer Avenue, Florida, 1709, South Africa
[4]Department of Theoretical Chemistry, University of Duisburg-Essen, Universitätstr. 2, D-45141, Essen, Germany

Abstract

Density-functional theory (DFT) has been used to calculate the electronic structures and magnetization in nanoporous graphene. We consider single nanopore (consisting of up to ten vacancies) and interacting nanopores (consisting in vacancy pairs, divacancy pairs and vacancy-divacancy pairs) separated at varying distances. We have notice that the interactions between the nanopores weaken as their separation distance increase and the formation energy tends to the value of single nanopore whereas the magnetic moment tends to the sum of individual ones. We proposed an empirical model for predicting the total magnetic moment as a function of nanopore size. This model is able to predict the magnetic moment of small and large nanopore sizes.

Computational Model

- Quantum ESPRESSO first-principles simulation package [1, 2] has been used for all the calculations.
- Interaction between the nuclei and the electrons is modeled by ultrasoft pseudopotentials [4], and the exchange-correlation functional is modeled GGA-PBE [3].
- A 10a × 10a (a = 2.46 Å) hexagonal graphene supercell of 200 carbon atoms to model our nanoporous defects.
- Two different nanoporous graphene structures containing single nanopores S_i i = 1, 2, 3, ...10 and those with double nanopores S_iS_j (i, j) = (1, 1), (1, 2), (2, 1), (2, 2) . The indices i and j stand for the number of carbon vacancy.

Result and discussion

We calculate the formation energy of all our structures and we obtain values in agreement with others DFT calculations. Throught the sum of local partial density of states (LPDOS) calculations and the electron spin density of all our structures we notice the extent of Carbon vacancies on the electronic and magnetic properties of graphene.
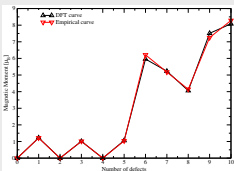

Fig. 1: Magnetic moments calculated from DFT (black curve) and obtained from the empirical equation (2) (red curve). [5]

We establish a relationship between the single nanoporous graphene ground-state magnetic moment and the number of dangling bonds presents in the nanopore by an empirical equation :

$$\mu_{V_n} = N_{DB}\left(1 + |\epsilon_{V_n}|\right)\mu_B \qquad (1)$$

N_{DB} is the number of carbon atoms containing the dangling bonds, μ_B is the Bohr magneton and ϵ_{V_n} a dimensionless real number ($|\epsilon_{V_n}| < 1$), calculated as function of vacancy defects's number n :

$$\epsilon_{V_n} = exp(-n/a_0) - a_2 * sin(\pi\, n + a_1) + a_3 \qquad (2)$$

$a_0 = 0.509306$, $a_1 = -0.123454$, $a_2 = 0.204424$ and $a_3 = 0.04$.
Moreover, our model is applies for large nanopore sizes and give good results, this has been tested for 22, 30 and 40 nanopores sizes and were in agreement with DFT results (see Table I).
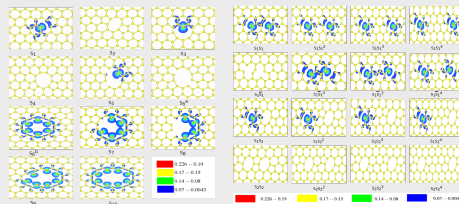
Single nanoporous graphene structures

Fig.2 : Spin density distribution around single nanoporous graphene structures. The nanoporous structure S_i^g differs to S_i^g by the geometrical form. (Right) Spin density distribution around the double nanoporous structures. [5].)

The calculated Local partial Density of states (LPDOS) of carbons atoms neighboring the nanopore, the 2p and 2s orbitals of S_1, S_3, S_5, S_6^g, S_7, S_8, S_9 and S_{10} nanostructures exhibit asymmetric DOS between spin-up and spin-down electrons. This can be explained by the fact that electron spins of carbon atoms neighboring each nanopore are aligned by exchange interactions which leads to a magnetic moments of 1.22, 1.01, 1.06, 5.96, 5.23, 4.06, 7.51 and 8.08 μ_B, respectively.

σ and π dangling bonds remains after the creation of the nanopores are responsible of the induced magnetism. The structures S_2, S_4 and S_6^g the 2p and 2s orbitals exhibit perfect symmetrical spin-up and spin-down DOS,

Table 1

The formation energy E_f and the total magnetic moment μ_{DFT} calculated from our DFT simulations, the estimated value μ_{V_n} calculated from equation (2) for the different nanostructures. These values are compared with previous DFT calculations E_f^i and μ^*. N_{DB} is the number of carbon atoms containing the dangling bonds while the dimensionless real numbers ϵ_{DFT} and ϵ_{V_n} are calculated from equation (2) for $\mu_{V_n} - \mu_{DFT}$ and the polynomial of equation (3) respectively. The notation for the defect systems has been described in the text.

System	n	$E_f(eV)$	$E_f^i(eV)$	N_{DB}	$\mu_{DFT}(\mu_B)$	$\mu_{V_n}(\mu_B)$	$\mu^*(\mu_B)$	$|\epsilon_{DFT}|$	$|\epsilon_{V_n}|$
S_1	1	7.55	7.65 [16], 7.60 [19]	1	1.22	1.22	1.33 [16], 1.16 [19]	0.220	0.220
S_2	2	3.68	4.50 [18]	0	0.00	0.00	0.00 [18]	–	0.018
S_3	3	3.55	3.96 [18]	1	1.01	1.01	1.02 [18]	0.010	0.011
S_4	4	2.72	3.30 [18]	0	0.00	0.00	0.00 [18]	–	0.055
S_5	5	2.95	–	1	1.06	1.05	–	0.060	0.050
S_6^g	6	2.71	2.72 [18]	0	0.00	0.00	–	–	–
S_6^g	6	2.81	2.87 [18]	6	5.96	6.12	6.00 [18]	0.006	0.021
S_7	7	2.57	–	5	5.23	5.06	–	0.046	0.012
S_8	8	2.48	–	4	4.06	4.15	–	0.015	0.038
S_9	9	2.43	–	7	7.51	7.45	–	0.073	0.065
S_{10}	10	2.26	–	8	8.08	8.08	–	0.010	0.011
S_{22}	22	1.68	–	4	4.01	4.09	–	0.003	0.022
S_{30}	30	1.27	–	12	12.32	12.30	–	0.026	0.025
S_{44}	44	0.99	–	8	8.13	8.23	–	0.016	0.029
S_1S_1	2	7.27	–	2	2.55	–	–	–	–
$S_1\overline{S}_1^i$	2	7.47	–	2	2.77	–	–	–	–
$S_1\overline{S}_1^j$	2	7.49	–	2	2.58	–	–	–	–
$S_1\overline{S}_1^g$	2	7.49	–	2	2.49	–	–	–	–
$S_1\overline{S}_1$	2	5.03	–	0	0.00	–	–	–	–
$S_1\overline{S}_1^g$	2	7.52	–	2	1.98	–	–	–	–
$S_1\overline{S}_1^j$	2	7.45	–	2	2.22	–	–	–	–
$S_1\overline{S}_1^g$	2	7.49	–	2	2.35	–	–	–	–
S_1S_2/S_2S_1	3	3.45/7.09	–	1	1.16	–	–	–	–
$S_1S_2^i/S_2S_1^i$	3	3.61/7.41	–	1	1.36	–	–	–	–
$S_1S_2^j/S_2S_1$	3	3.62/7.42	–	1	1.21	–	–	–	–
$S_1S_2^g/S_2S_1^g$	3	3.62/7.44	–	1	1.22	–	–	–	–
S_2S_2	4	2.91	–	0	0.00	–	–	–	–
$S_2S_2^g$	4	3.34	–	0	0.00	–	–	–	–
$S_2S_2^j$	4	3.50	–	0	0.00	–	–	–	–
$S_2S_2^g$	4	3.57	–	0	0.00	–	–	–	–

Electron spin densities presented above (Fig. 2), revealed that the magnetization is concentrated on C atoms around nanopores.
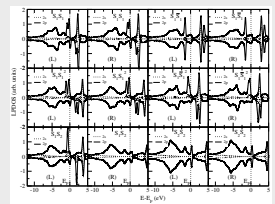
Double nanoporous graphene structures

Fig. 4: Sum of local partial density of states (LPDOS) 2p and 2s for the carbon atoms surrounding each single nanopore belonging to S_1S_1, $S_1\overline{S}_1$, S_1S_2, S_2S_2, $S_1\overline{S}_1^i$ and $S_1S_1^j$. (L) and (R) stand for the left and right nanopores in these double structures

The formation energy is lesser than that of single nanopore.
However, as the separation between nanopore increases, the formation energy tends to that of isolated nanopore.
The structure $S_1\overline{S}_1$ is made of single magnetic nanopores S_1 but it's has zero magnetic moment (see Fig. 4).

Conclusion

- Induced magnetism by carbon vacancy defects in single and interacting nanopores is related to the presence of σ and π dangling bonds resulting from the creation of the vacancies making up the nanopores.
- Our empirical model predicts the total magnetic moment in single nanoporous graphene in good agreement with the DFT values.
- The interactions between nanopores in graphene play a fundamental role in its magnetic behavior.
- The magnetic properties of individual nanopores participating in the interactions appear to also have an impact on the magnetization.
- The nanopores may interact with each others resulting in an increase or total annihilation of the magnetic moment.

Acknowledgements

References

[1] Paolo Giannozzi, Stefano Baroni, et al., Quantum espresso: a modular and open-source software project for quantum simulations of materials, J. Phys. Condens. Matter 21 (39) (2009) 395502

[2] Paolo Giannozzi, Oliviero Andreussi, et al., Advanced capabilities for materials modelling with quantum espresso, J. Phys. Condens. Matter 29 (46) (2017) 465901.

[3] John P. Perdew, Kieron Burke, et al. Generalized gradient approximation made simple, Phys. Rev. Lett. 77 (18) (1996) 3865.

[4] David Vanderbilt, Soft self-consistent pseudopotentials in a generalized eigenvalue formalism, Phys. Rev. B 41 (11) (1990) 7892.

[5] F. B. S. Nkou, D. H. Douma, et al., Theoretical insights into magnetization in graphene containing single and interacting nanoporous defects, Physica E: Low-dimensional Systems and Nanostructures 128 (2020) 114564

Influence of concentration of anthocyanins on electron transport in dye sensitized solar cells

The influence of concentration of anthocyanins in dye sensitized solar cells (DSSC) has been investigated, with focus on how concentration influence electron transport. The influence on electron transport was then linked solar cell performance. Anthocyanins were extracted from fresh flowers of Acanthus pubscenes using methanol acidified with 0.5% trifluoracetic acid, concentrated using a rotary evaporator and partitioned against ethyl acetate. Concentration of the anthocyanins was determined using Keracyanin Chloride as a standard. DSSC were fabricated using Titanium dioxide as anode, anthocyanins as sensitizers and Platinum as counter electrode material. Titanium dioxide was deposited on Fluorine doped Tin oxide glass substrate using slot coating method. Platinum was deposited on FTO glass substrate using a brush previously dipped in plastisol precursor, and annealed a t 450 0C for 20 minutes to activate Platinum. Dye sensitized solar cells were assembled using anthocyanins at varying concentrations. Performance parameters of the solar cells were measured using a solar simulator which was fitted with digital source meter. Electron transport parameters were studied using electrochemical impedance spectroscopy (EIS). Open circuit voltage, short circuit current and fill factor were observed to increase with concentration of anthocyanins. The increase in solar cell performance was attributed to increase in charge density which led more charges being available for transported to solar cell contacts. The increased charge resulted in a negative shift in Fermi level of electrons in the conduction band of TiO_2. The shift in Fermi level resulted into an increase in open circuit voltage and the overall solar cell performance. EIS studies revealed increase in recombination resistance with concentration of anthocyanins. The increase in recombination resistance was found to be related to increase in electron density, and hence the shift in the Fermi level of electrons in the conduction band of TiO_2. Key words: Dye sensitized solar cells; TiO_2; Impedance Electron Spectroscopy; slot coating; Fermi level; Recombination resistance; Electron lifetime.

Quasi-two-dimensional electron and hole gases at the head-to-head and tail-to-tail 180° domain walls in ferroelectric thin films

In recent years, many scholars have proposed numerous schemes on screening of bound charges and stabilization of head-to-head (HH) and tail-to-tail (TT) 180° domain walls in ferroelctrics. By use of first-principles, most research groups employed (i) substitutional atoms at one or two HH and TT domain walls in superlattices, (ii) altering defect concentration at the tails in a thin films. However, such approaches say nothing regarding the intrinsic critical thickness for the stabilization of the two-dimensional conducting layers for screening of polarization charges, the spatial extend in which the hole and electron gases cover nor the magnitude extend of polarization if the said domain walls would be induced in a slab. % Using density functional calculations, we show how we were able to stabilize 180° head-to-head and tail-to-tail domains in the out-of-plane monodomain configuration in PbTiO$_3$ thin films grown on SrTiO$_3$ substrate. This was possible without the aid of dopants nor vacancies, but solely electrostatic screening emanating from free carriers. Our findings illustrate the widths of the of the domain wall of around 6 unit cells for HH and 7 unit cells for TT. Equally deduced from our calculation, was the perfect match between the density of free charge and the polarization profile. % These findings support the existence of an extra source of charge at the domain walls to explain the enhancement of the conductivity observed in some domains walls of prototypical, insulating in bulk, perovskite oxides.

Computational study of chlorine-ion adsorption on Ti (100) surface

Etching process is becoming essential and the most advanced technique for removing alpha-case layer in material production. The adsorption of ion species is the major relevance for metal surface etching because the mechanism is brought by metal-ion interaction. Even though the ions play an important role in metal surface processing, the studies remain limited and challenging, especially at the atomistic scale. In this work first-principle approach is used to investigate the structural and electronic properties of Cl2 molecule adsorption on Ti (100) surface at different coverage. The present results revealed that adsorption of Cl2 molecule is by dissociation with Ti-Cl bonding. Therefore, the calculated adsorption energy denotes an exothermic reaction with the hollow site being the most stable adsorption position. Increasing the Cl2 coverage resulted in volatile titanium halides (TiCl4 and Ti2Cl6) with a negative value of formation energy. All the formed volatile molecules were found detaching from the Ti (100) surface. The calculated desorption energy possesses a positive energy barrier with TiCl4 molecule possessing a lower energy barrier than Ti2Cl6. This suggests that the atomic layer etching on Ti surface happened by desorption of TiCl4 whereby the amount of material removed is etch per TiCl4 formed. Also, partial density of states (PDOS) plots and charge density redistribution were studied to analyze the electronic properties.

Structural and Electronic Calculation of Tungsten Disulfide Using Density Functional Theory

The structural and electronic properties of mono layer tungsten disulfide (WS_2) are investigated using first principle calculation. The unknown exchange correlation functional are approximated with generalized gradient approximation. The convergence test of total energy with respect to energy cutoff and k-point sampling is performed to assure the accuracy of calculations. The equilibrium lattice constant of mono layer WS2 is calculated and with 1.6% error. Moreover, the electronic band it is in good agreement with experimental values. Its value is 3.23 A. Moreover, the band structure and density of states of mono layer WS2 are determined computationally and compared with experimental result. The calculated value of band gap is 1.875 eV with percentage error of 6.25% from experimental value. The density of state (DOS) calculation helps to understand the electronic transport property of the system.